Support Information

1. The content of Zn and Fe in the $Zn_xFe_{3-x}O_4$ NPs

The ICP-OES technique was employed to examine the correspondence between the actual Zn and Fe contents in the final samples and their respective theoretical values at various Zn doping levels, obtained results are presented in Table S1.

Table S1: The real content of Zn doping in the $Zn_xFe_{3-x}O_4$ by ICP-OES (Rr: real ratio of Fe and Zn content, Tr: theoretical ratio of Fe and Zn content).

Sample	CZn(mM)	CFe(mM)	Rr	Tr
$Zn_{0.1}$	3.00	148.50	49.50	29.00
$Zn_{0.2}$	8.10	147.00	18.15	14.00
$Zn_{0.3}$	21.35	153.00	7.17	9.00
$Zn_{0.4}$	23.00	150.00	6.52	6.50
$Zn_{0.5}$	25.55	130.00	5.09	5.00

2. **The bulk density (ρ_b) and estimated X-ray density (ρ_{XRD}) as a function of $Zn_xFe_{3-x}O_4$**
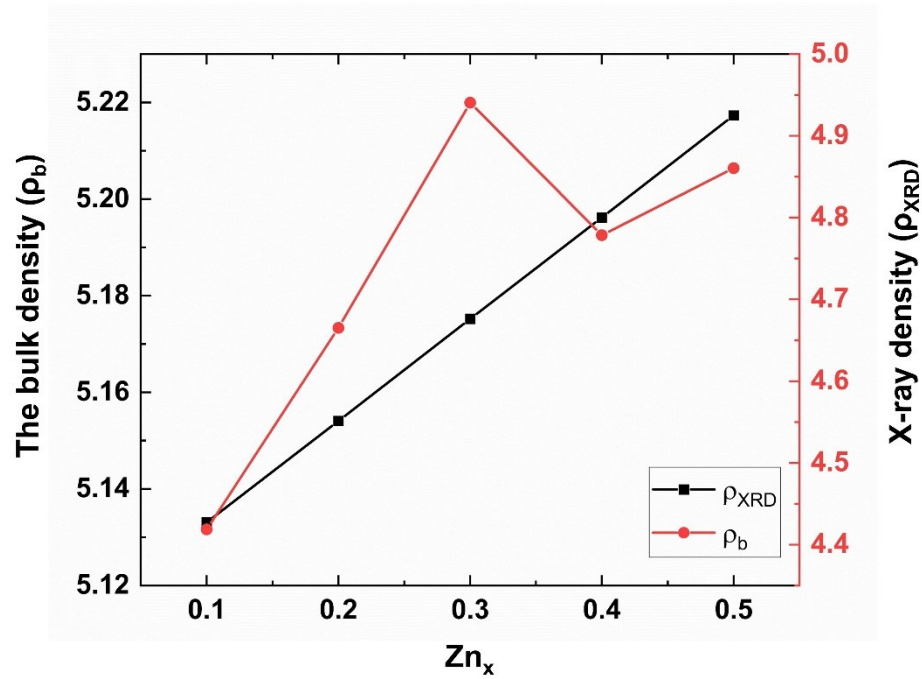

Figure S1: The bulk density (ρ_b) and the estimated X-ray density (ρ_{XRD}) as a function of $Zn_xFe_{3-x}O_4$ NPs (x = 0.1, 0.2, 0.3, 0.4, and 0.5).

3.   NP's stiffness evaluation by cation's distribution mathematic analysis

Porosity (P %) and Poisson's ratio (σ) were determined depending on the X-ray density (ρ_{XRD}) (obtained using the Rietveld refinement of XRD results) and the measured bulk density (ρ_b) by these equations:

$$P(\%) = \left(1 - \frac{\rho_b}{\rho_{XRD}}\right) * 100 \qquad (S1)_1$$

$$\sigma = 0.324 * (1 - 1.043 * P) \qquad (S2)_2$$

These force constants (ko) and (kt) are determined utilizing the Waldron equations:[3]

$$K_t = 7.62 * M_1 * v_1^2 * 10^{-2} \qquad (S3)$$

$$K_o = 10.62 * \frac{M_2}{2} * v_2^2 * 10^{-2} \qquad (S4)$$

where M_1 and v_1 are the molecular weight and the absorption band of the tetrahedral site, respectively. M_2 and v_2 are the molecular weight and the absorption band of the octahedral site, respectively.

Elastic constants (C_{11}) and (C_{12}) are related to force constants (k_o) and (k_t) and Poisson ratio (σ) and are defined by the these equations:[4]

$$C_{11} = \frac{k_{av}}{a} \qquad (S5)$$

$$C_{12} = \frac{C_{11} * \sigma}{(1 - \sigma)} \qquad \text{(S6)}$$

$$k_{av} = \frac{K_t + K_o}{2} \qquad \text{(S7)}$$

The following relationships can be utilized for calculating the different elastic moduli, namely Young's modulus (E), bulk modulus (B), and rigidity modulus (G):[3]

$$E(GPa) = \frac{(C_{11} - C_{12}) * (C_{11} + 2 * C_{12})}{(C_{11} + C_{12})} \qquad \text{(S8)}$$

$$B(GPa) = \frac{1}{3} * (C_{11} + 2 * C_{12}) \qquad \text{(S9)}$$

$$G(GPa) = \frac{E}{2 * (\sigma + 1)} \qquad \text{(S10)}$$

4. NP's stiffness evaluation by Single-molecule force spectrometry of atomic force microscopy (SMFS-AFM)

Utilizing AFM scanning mode, topological images were acquired to visualize the individual locations of NP's samples with varying Zn-content (x). Subsequently, we transitioned to the shoot mode in Nanoscope V9.3 Software. In the shoot mode, 15 shots were taken for each NP by manually selecting the center of each NP using the crosshair tool. Force was then applied, and the software recorded 15 deflection-displacement curves for each NP, with a minimum of 60 NPs analyzed for each Zn-content (x). **Figure S2** depicts one of these deflection-displacement curves. Deflection-displacement curves have been bassline correlation then fitted by indentation function using MountainsLab 9 (Digital Surf, France) software.
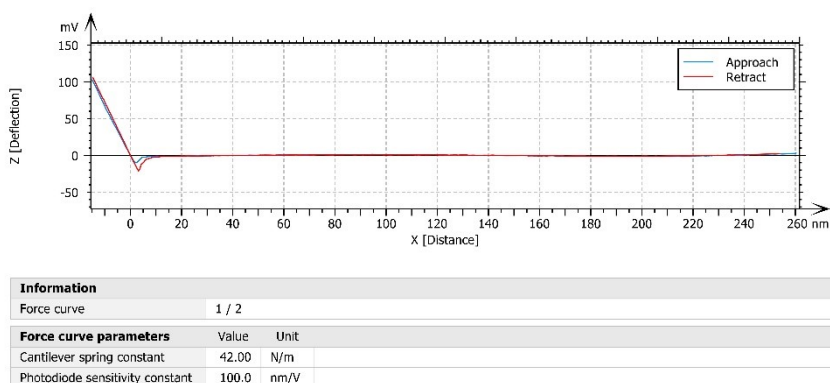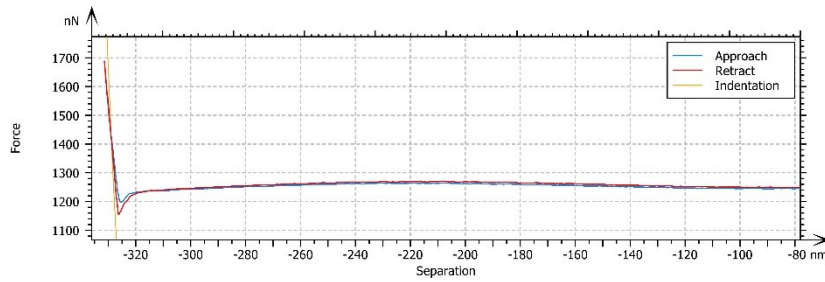

Information		
Force curve	1 / 2	
Force curve parameters	Value	Unit
Cantilever spring constant	42.00	N/m
Photodiode sensitivity constant	100.0	nm/V

Figure S2: Sample of deflection-displacement curves

Information		
Force curve	1 / 2	
Force curve parameters	Value	Unit
Cantilever spring constant	42.00	N/m
Photodiode sensitivity constant	100.0	nm/V
Cursor sets	X0-X1	Unit
Force difference	1.575	nN
Separation difference	2.139	nm
Slope	0.7364	nN/nm
Indentation parameters	I0	Unit
Tip shape	Conical	
Half pyramid angle	16.00	°
Young's modulus	31.81	GPa
Point of zero indentation (I0)	-315.4	nm
Coefficient of determination R²	0.000	

Figure S3: Sample of force-indentation curves fitted from deflection-displacement curves using the indentation function enables us to calculate Young's modulus.

The Indentation function enables the fitting of deflection-displacement curves to obtain force-indentation curves and calculate Young's modulus, **Figure S3** pres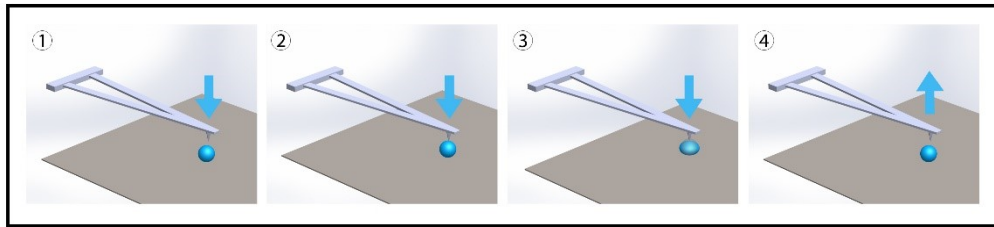ents one of these force-indentation curves. **Figure S4** presents the sequential steps involved in AFM Single Molecule Force Spectrometry (AFM-SMFS), accompanied by the corresponding deflections of the AFM cantilever recorded on the diagram in **Figure S5** for each step. The force-indentation curve obtained from AFM-SMFS is influenced by the indentation process. 1) Initially, the probe approaches the NP while the force keeps at zero. 2) The probe tip starts indenting the NP, resulting in a gradual increase in force in minus direction cues the contact force act from NPs to the cantilever. 3) The indentation continues and the cantilever uploads compress force on NPs leading to a faster increase in force,

indicated by a steeper slope.[5,6] The conical indenter model, developed by Sneddon,[7] was applied for the conical tip cantilever as the scheme in **Figure S5** shown and the Sneddon equation as follows:

$$F = \frac{2}{\pi} * \frac{E}{(1 - v^2)} * \delta^2 * tan(\alpha)$$

(S11)

Where F, E, δ, α, and v represent force, Young's modulus, indentation, conical tip's half angle, and Poison's ratio, respectively.

Figure S4: The sequential steps involved in AFM Single Molecule Force Spectrometry (AFM-SMFS).
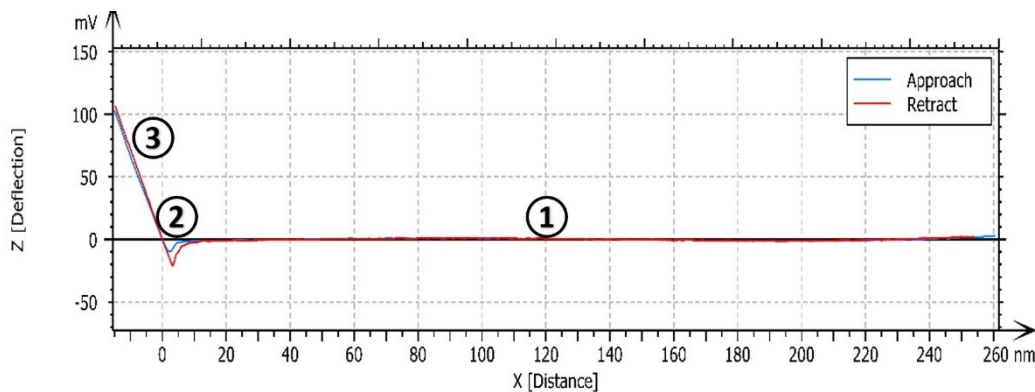

Figure S5: The corresponding deflections of the AFM cantilever involved in AFM Single-Molecule Force Spectrometry (AFM-SMFS).
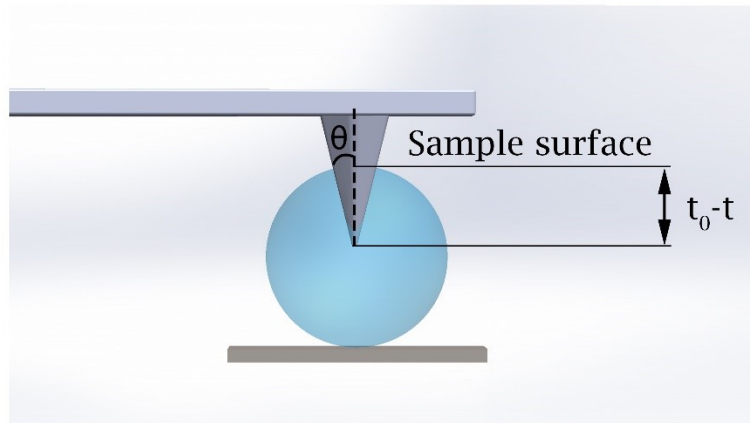
Figure S6: Sample of force-indentation curves fitted from deflection-displacement curves using the Indentation function enables us to calculate Young's modulus.

The force-distance curve (**Figure S5**) obtained during force spectroscopy measurements captures the probe's response during the approach-retract cycle. The extension half of the curve represents the tip approaching and making contact with NPs, while the retraction half measures the adhesion event between the tip and NPs. The extension curve showed two regimes with a sharp transition between these two regions at point 2 in **Figure S5**, a flat horizontal approach (point 1 - point 2), and a steep linear deflection (point 2 - point 3) with a slope used to determine.[8,9]

Certain force-distance curves were excluded from the analysis based on specific criteria. Curves were disregarded if they exhibited exceptionally high stiffness when the tip did not accurately contact the center of the NPs, leading to contact with the substrate. Similarly, curves were discarded if they yielded unacceptably low stiffness values due to lateral motion occurring when the tip made contact

with the side of the spheres. These exclusions were implemented to guarantee the reliability and precision of the collected data.

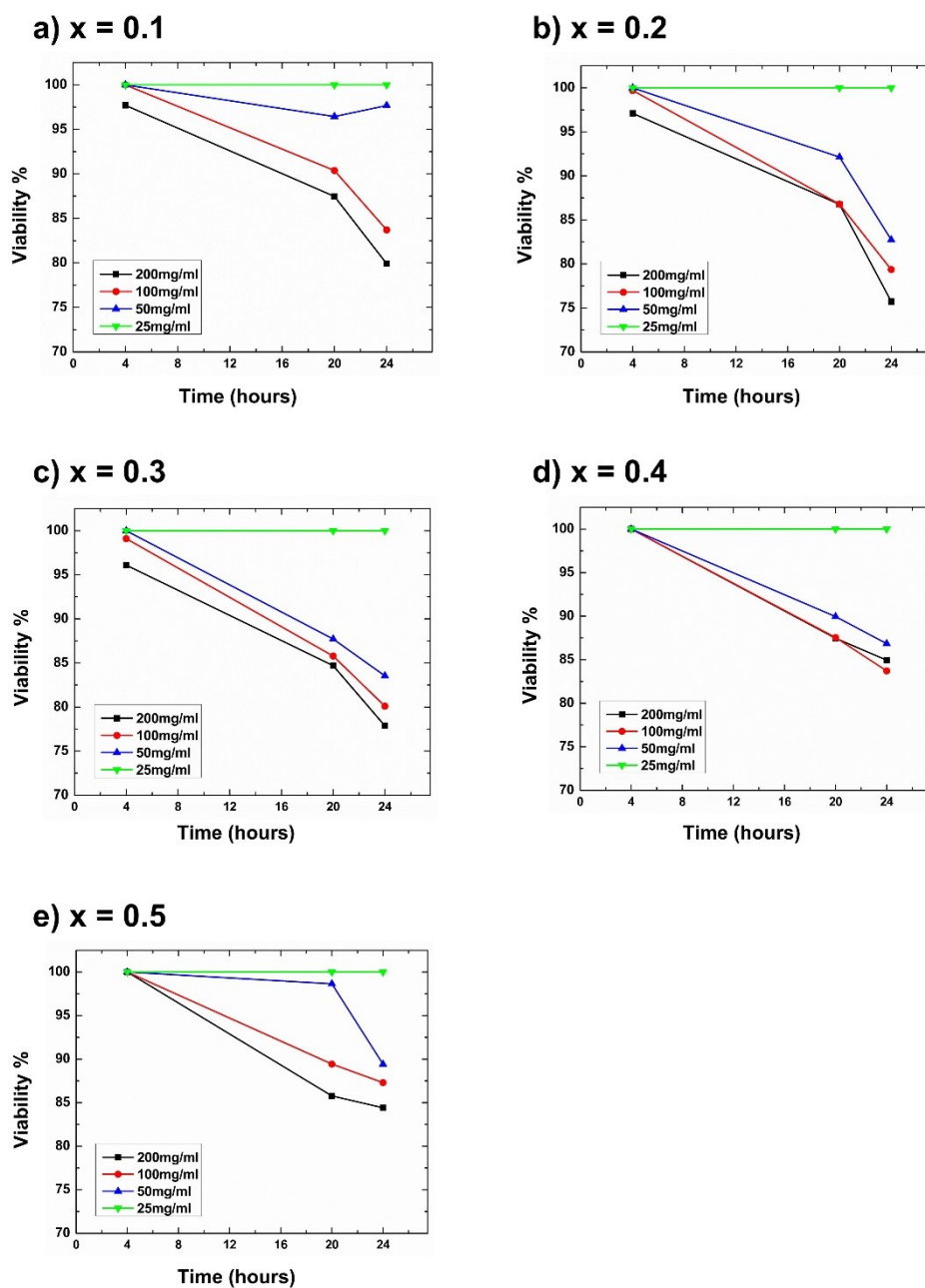## 5.   Effect of NP's stiffness on cell viability

Figure S7: Cellular viability of MCF-7 cells at different concentrations (25, 50, 100, 200 μg/mL) of $Zn_xFe_{3-x}O_4$ NPs and different Zn doped content. a) (x = 0.1), b) (x = 0.2), c) (x = 0.3), d) (x = 0.4), and e) (x = 0.5).
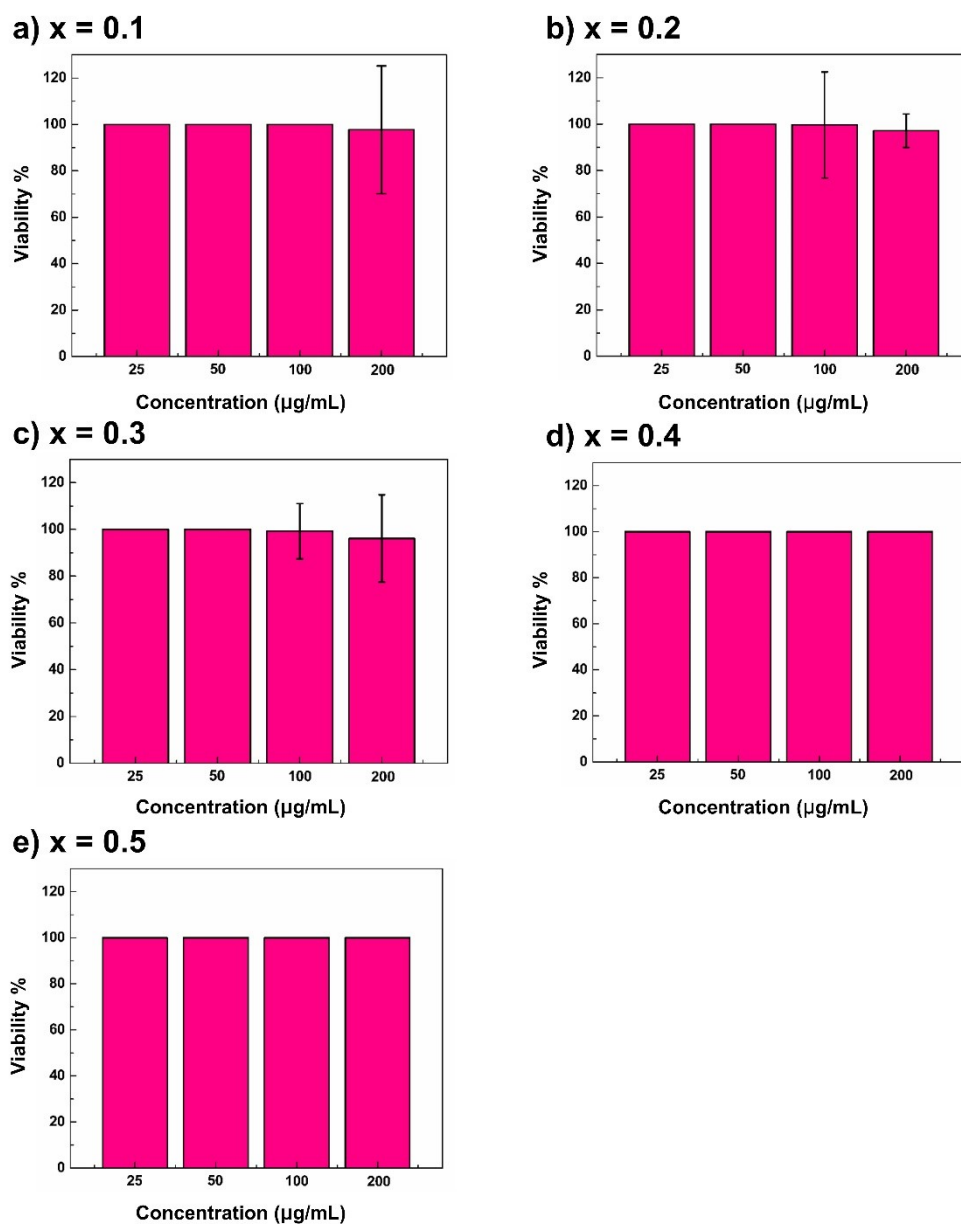
Figure S8: Cell viability of MCF-7 cells at different concentrations of $Zn_xFe_{3-x}O_4$ NPs (25, 50, 100, 200 μg/mL) after 4 hours and different Zn doped content. a) (x = 0.1), b) (x = 0.2), c) (x = 0.3), d) (x = 0.4), and e) (x = 0.5).
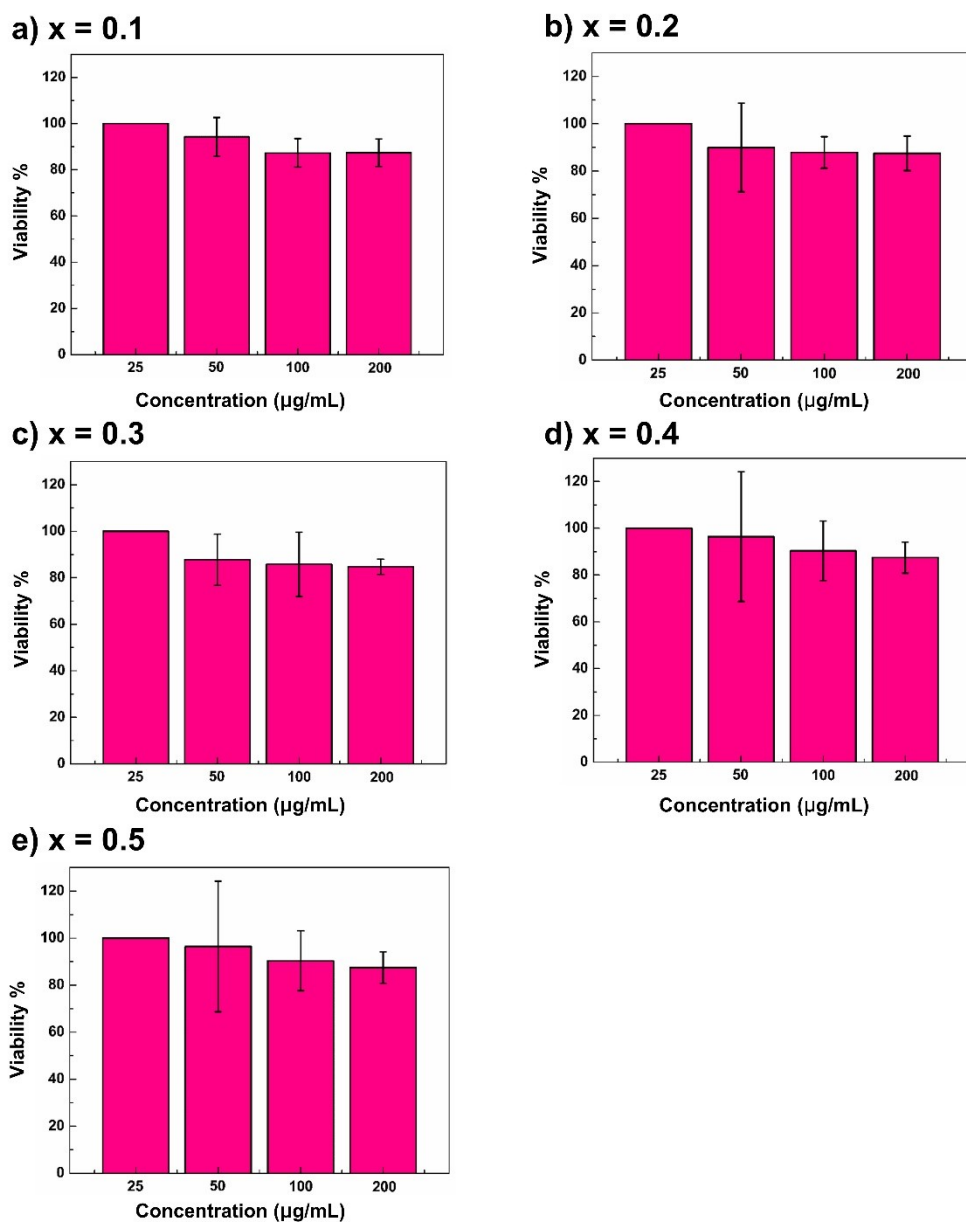
Figure S9: Cell viability of MCF-7 cells at different concentrations (25, 50, 100, 200 µg/mL) of $Zn_xFe_{3-x}O_4$ NPs after 20 hours and different Zn doped content. a) (x = 0.1), b) (x = 0.2), c) (x = 0.3), d) (x = 0.4), and e) (x = 0.5).

Figure S10: Cell viability of MCF-7 cells at different concentrations (25, 50, 100, 200 μg/mL) of $Zn_xFe_{3-x}O_4$ NPs after 24 hours and different Zn doped content. a) (x = 0.1), b) (x = 0.2), c) (x = 0.3), d) (x = 0.4), and e) (x = 0.5).
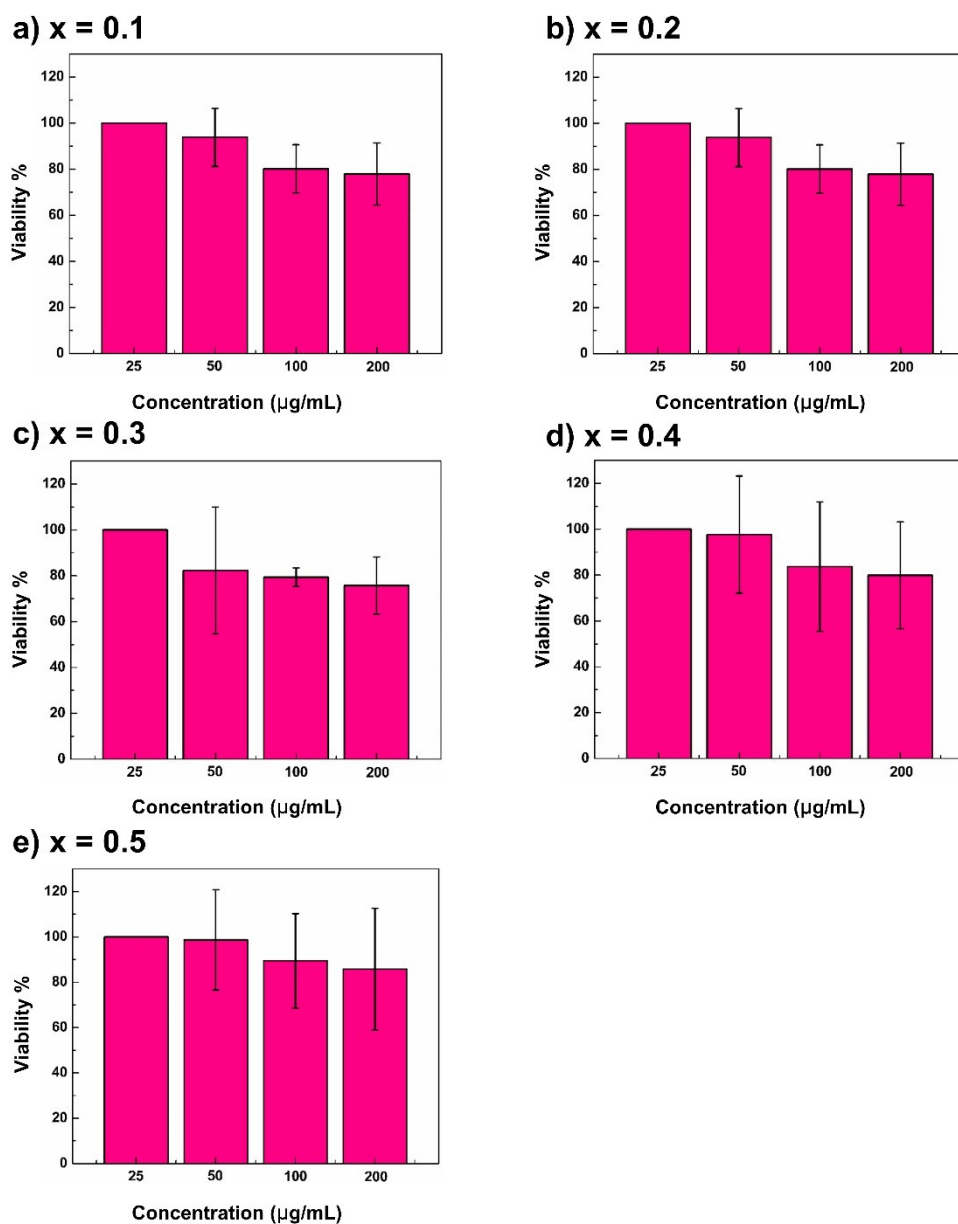
REFERENCES

(1)   Islam, M. A.; Hossain, A. K. M. A.; Ahsan, M. Z.; Bally, M. A. A.; Ullah, M. S.; Hoque, S. M.; Khan, F. A. Structural Characteristics, Cation Distribution, and Elastic Properties of Cr3+ Substituted Stoichiometric and Non-Stoichiometric Cobalt Ferrites. RSC Adv. 2022, 12 (14), 8502–8519. https://doi.org/10.1039/d1ra09090a.

(2)   Tatarchuk, T. R.; Paliychuk, N. D.; Bououdina, M.; Al-Najar, B.; Pacia, M.; Macyk, W.; Shyichuk, A. Effect of Cobalt Substitution on Structural, Elastic, Magnetic and Optical Properties of Zinc Ferrite Nanoparticles. J. Alloys Compd. 2018, 731, 1256–1266. https://doi.org/10.1016/j.jallcom.2017.10.103.

(3)   Mohamed, M. B.; Wahba, A. M. Structural, Magnetic, and Elastic Properties of Nanocrystalline Al-Substituted Mn0.5Zn0.5Fe2O4 Ferrite. Ceram. Int. 2014, 40 (8 PART A), 11773–11780. https://doi.org/10.1016/j.ceramint.2014.04.006.

(4)   El-Ghazzawy, E. H.; Amer, M. A. Structural, Elastic and Magnetic Studies of the as-Synthesized Co1−xSrxFe2O4nanoparticles. J. Alloys Compd. 2017, 690, 293–303. https://doi.org/10.1016/j.jallcom.2016.08.135.

(5)   Del Pino, P.; Yang, F.; Pelaz, B.; Zhang, Q.; Kantner, K.; Hartmann, R.; Martinez De Baroja, N.; Gallego, M.; Möller, M.; Manshian, B. B.; Soenen, S. J.; Riedel, R.; Hampp, N.; Parak, W. J. Basic Physicochemical Properties of Polyethylene Glycol Coated Gold Nanoparticles That Determine Their Interaction with Cells. Angew. Chemie - Int. Ed. 2016, 55 (18), 5483–5487. https://doi.org/10.1002/anie.201511733.

(6)   Wang, L.; Jang, G.; Ban, D. K.; Sant, V.; Seth, J.; Kazmi, S.; Patel, N.; Yang, Q.; Lee, J.; Janetanakit, W.; Wang, S.; Head, B. P.; Glinsky, G.; Lal, R. Multifunctional Stimuli Responsive Polymer-Gated Iron and Gold-Embedded Silica Nano Golf Balls: Nanoshuttles for Targeted on-Demand Theranostics. Bone Res. 2017, 5 (August), 1–14. https://doi.org/10.1038/boneres.2017.51.

(7)   Sneddon, I. N. The Relation between Load and Penetration in the Axisymmetric Boussinesq Problem for a Punch of Arbitrary Profile. Int. J. Eng. Sci. 1965, 3 (1), 47–57. https://doi.org/10.1016/0020-7225(65)90019-4.

(8)   Hui, Y.; Yi, X.; Wibowo, D.; Yang, G.; Middelberg, A. P. J. J.; Gao, H.; Zhao, C. X. Nanoparticle Elasticity Regulates Phagocytosis and Cancer Cell Uptake. Sci. Adv. 2020, 6 (16), 1–11. https://doi.org/10.1126/sciadv.aaz4316.

(9)   Ramalingam, B.; Parandhaman, T.; Das, S. K. Antibacterial Effects of Biosynthesized Silver Nanoparticles on Surface Ultrastructure and Nanomechanical Properties of Gram-Negative Bacteria Viz. Escherichia Coli and Pseudomonas Aeruginosa; 2016; Vol. 8. https://doi.org/10.1021/acsami.6b00161.